Volume 5
Number 17
7 September 2023
Pages 4301–4612

Nanoscale Advances

rsc.li/nanoscale-advances

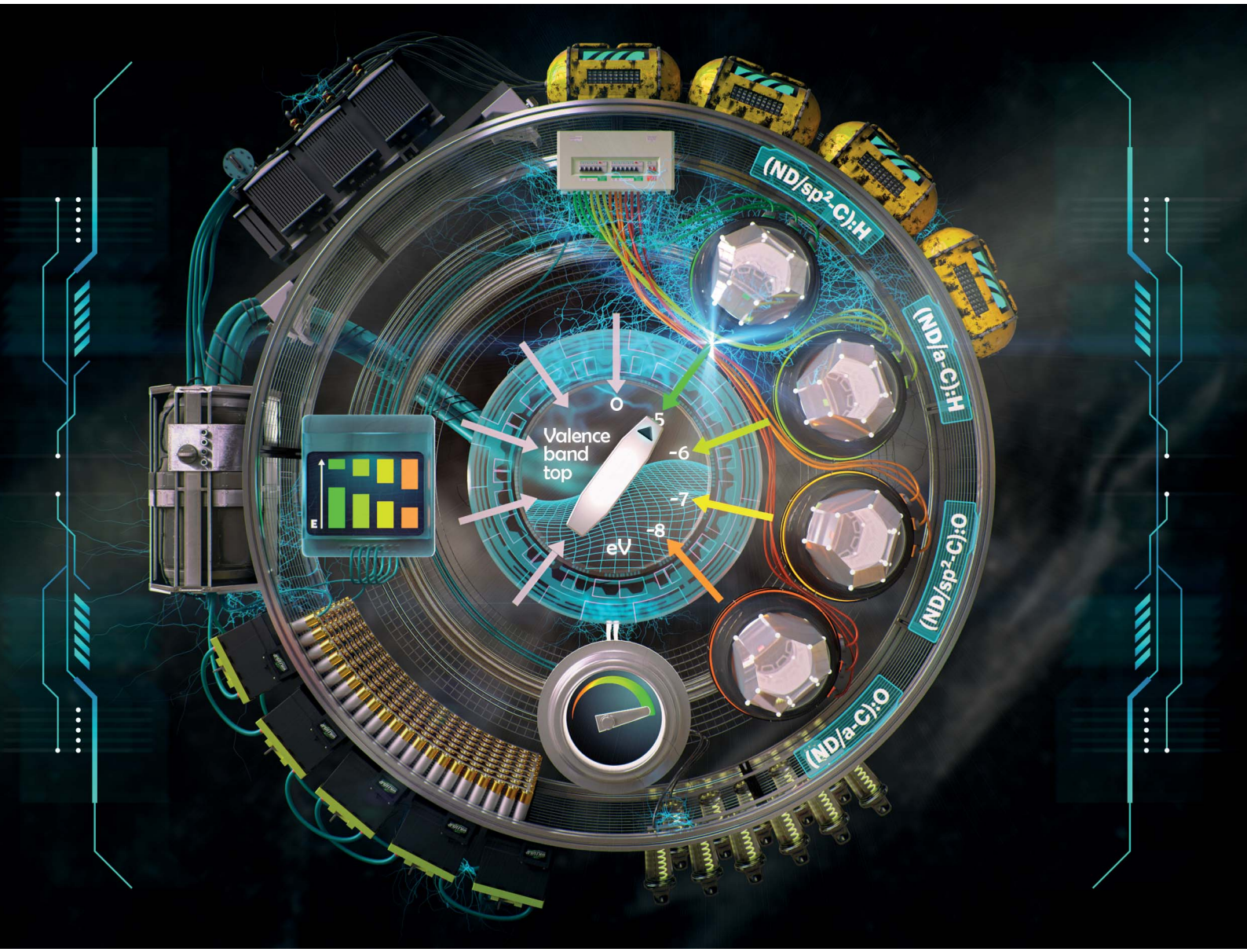

ISSN 2516-0230

ROYAL SOCIETY OF CHEMISTRY

PAPER
Daria Miliaieva *et al.*
Absolute energy levels in nanodiamonds of different origins and surface chemistries

NCNST

Nanoscale Advances

ROYAL SOCIETY OF CHEMISTRY

PAPER

View Article Online
View Journal | View Issue

Cite this: *Nanoscale Adv.*, 2023, **5**, 4402

Absolute energy levels in nanodiamonds of different origins and surface chemistries†

Daria Miliaieva, *[ae] Aurelien Sokeng Djoumessi,[bc] Jan Čermák,[a] Kateřina Kolářová,[a] Maximilian Schaal,[d] Felix Otto,[d] Ekaterina Shagieva,[a] Olexandr Romanyuk,[a] Jiří Pangrác,[a] Jaroslav Kuliček,[e] Vojtech Nádaždy,[fg] Štěpán Stehlík,[ah] Alexander Kromka,[a] Harald Hoppe[bc] and Bohuslav Rezek[e]

Nanodiamonds (NDs) are versatile, broadly available nanomaterials with a set of features highly attractive for applications from biology over energy harvesting to quantum technologies. *Via* synthesis and surface chemistry, NDs can be tuned from the sub-micron to the single-digit size, from conductive to insulating, from hydrophobic to hydrophilic, and from positively to negatively charged surface by simple annealing processes. Such ND diversity makes it difficult to understand and take advantage of their electronic properties. Here we present a systematic correlated study of structural and electronic properties of NDs with different origins and surface terminations. The absolute energy level diagrams are obtained by the combination of optical (UV-vis) and photoelectron (UPS) spectroscopies, Kelvin probe measurements, and energy-resolved electrochemical impedance spectroscopy (ER-EIS). The energy levels and density of states in the bandgap of NDs are correlated with the surface chemistry and structure characterized by FTIR and Raman spectroscopy. We show profound differences in energy band shifts (by up to 3 eV), Fermi level position (from p-type to n-type), electron affinity (from +0.5 eV to −2.2 eV), optical band gap (5.2 eV to 5.5 eV), band gap states (tail or mid-gap), and electrical conductivity depending on the high-pressure, high-temperature and detonation origin of NDs as well as on the effects of NDs' oxidation, hydrogenation, sp^2/sp^3 carbon phases and surface adsorbates. These data are fundamental for understanding and designing NDs' optoelectrochemical functional mechanisms in diverse application areas.

Received 30th March 2023
Accepted 16th June 2023

DOI: 10.1039/d3na00205e

rsc.li/nanoscale-advances

1 Introduction

Diamond nanoparticles, so-called nanodiamonds (NDs), are fascinating carbon-based nanomaterials, characterised by a rigid and stable diamond core and a reactive surface that can host multiple surface functional groups.[1–5] The diamond lattice in the ND core keeps the bulk-like diamond structure down to a few nm,[6] and allows the possibility to host stable colour centres such as nitrogen or silicon vacancies in sub-10 nm NDs.[7–9] In contrast, due to the extremely high surface-to-volume ratio, it is the surface chemistry that controls NDs' colloidal and, in particular, electronic properties as well as interactions with other materials including biosystems.[10–13] Oxidized and hydrogenated ND surfaces can be understood as two counterparts in terms of zeta potential sign as well as the remarkable difference in their work functions,[14] and electrical conductivities.[15] By analogy with experimental data on the negative electron affinity (NEA) of hydrogenated diamonds and the positive electron affinity (PEA) of oxidized diamonds,[16–18] the calculations for NDs show that hydrogenated (and hydroxylated while in vacuum) NDs possess NEA,[19,20] while oxidised NDs exhibit PEA.[20] Moreover, NEA in nanodiamonds falls into two classes due to the lattice strain. The first class with a low NEA between −3.3 eV and −4.5 eV is strongly size-dependent. The second class with the higher NEA between 0 eV and −2.0 eV depends on ND anisotropy, but not on size.[19]

[a]*Institute of Physics, Czech Academy of Sciences, Na Slovance 1999/2, 182 21 Prague 8, Czech Republic. E-mail: miliaieva@fzu.cz*
[b]*Center for Energy and Environmental Chemistry Jena (CEEC Jena), Friedrich Schiller University Jena, Philosophenweg 7a, 07743 Jena, Germany*
[c]*Laboratory of Organic and Macromolecular Chemistry (IOMC), Friedrich Schiller University Jena, Humboldstrasse 10, 07743 Jena, Germany*
[d]*Institute of Solid State Physics, Friedrich Schiller University Jena, Helmholtzweg 5, 07743 Jena, Germany*
[e]*Faculty of Electrical Engineering, Czech Technical University in Prague, 166 27 Prague, Czech Republic*
[f]*Institute of Physics, Slovak Academy of Sciences, Dúbravská cesta 9, 845 11 Bratislava, Slovak Republic*
[g]*Centre for Advanced Material Application, Slovak Academy of Sciences, Dúbravská cesta 9, 845 11 Bratislava, Slovak Republic*
[h]*New Technologies – Research Centre, University of West Bohemia, Univerzitní 8, 306 14, Pilsen, Czech Republic*

† Electronic supplementary information (ESI) available. See DOI: https://doi.org/10.1039/d3na00205e

Commercially available NDs often contain a non-diamond carbon phase (in the form of sp^2 or amorphous carbon) that, for example, significantly impacts the catalytical[21] or colloidal properties of NDs after hydrogenation.[22] This set of unique chemical and structural properties as well as the great modification window makes NDs promising in various energy-oriented applications. For example, the successful application of NDs has been reported in photo-[23,24] and electrocatalysis,[25] supercapacitors,[26] batteries[27] and in optoelectronics as electron emitters,[28] electrode substrates[29] and materials for solar cell components.[30,31]

For understanding the roles of NDs and the effects they may have on the optoelectronic applications, knowledge about their energy band structure is essential. Usually, energy levels of nanodiamonds are approximated by the energy levels of the bulk diamond[24,32] which may not be easily applicable due to the above-mentioned large variability in the ND material properties, namely the size, structure, and surface chemical properties. So far, only partial data and sometimes inconsistent data have been reported. In particular, only relative energy level shifts have been shown in NDs with oxidized and hydrogenated surface chemistry[14,33] and inconsistent values of ND electronic bandgaps were reported.[30,34] Also, support by theoretical approaches is limited to very small ND models due to the enormous computational cost of the larger ND particles. Here, by means of density functional theory (DFT) calculations, the energy diagrams for sub-1 nm NDs of different surface chemistries were constructed.[35] However, the direct applicability of the data obtained for such small NDs is questionable due to the inherent quantum confinement at this scale.[36]

This work presents the comprehensive opto-electronic-chemical study of the as-received, fully hydrogenated (reduced) and fully oxidized NDs. Certain variation of the ND structure is ensured by the employment of monocrystalline high-pressure high-temperature (HPHT) and "polycrystalline" and defective detonation NDs (DNDs). UV-visible, ultraviolet photoemission, and electrochemical impedance spectroscopies are combined with the Kelvin probe and the absolute values of the energy levels for NDs are presented and elaborated by the electronic density of states. The profound effect of the non-diamond phase in NDs of particular surface chemistries is discussed. Finally, the model comprising the combined effect of the surface chemistry and the carbon hybridisation on the energy levels is suggested which opens the way for predicting the ND behaviour in the prospective applications and explains the ND function mechanism in the reported optoelectronic applications.

2 Experimental part

2.1 Materials

Nanodiamonds of different origins and surface chemistries were the subjects of this study. NDs of detonation origin (DNDs) were purchased from New Metals and Chemicals Corp., Japan (purity >98%). The mean size of the primary DND particles is ~5 nm. This sample in the as-received state is further denoted as DND-ar. Monocrystalline high-pressure high-temperature (HPHT) NDs were purchased from Pureon, Switzerland. The size range is 0–30 nm and the mean size is ~18 nm, the least of the commercially available sizes for HPHT NDs. This sample in the as-received state is further labelled as HPHT ND-ar.

The surface annealing of NDs was performed with the optimal parameters to assure the fullest hydrogenation/oxidation keeping a similar size distribution to the as-received ND material[37] (Fig. S1†). To prepare oxidized DNDs, air annealing at 450 °C for 30 min was performed which leads to surface oxidation and purification;[38] longer annealing and/or higher temperature already leads to unwanted etching of the DNDs.[39,40] Due to an average larger size and monocrystalline structure, HPHT NDs can be nearly completely purified from the sp^2-C at 450 °C for 300 min.[41] This is the well-established and widely used (*i.e.* relevant) annealing procedure in the air that has been proven many times for cleaning and oxidation of the nanodiamond surface[42] and introduction of the carboxylic groups or their corresponding dehydrated forms—anhydrides on the ND surface.[43] The oxidized DNDs are denoted as DND-O and oxidized HPHT NDs as HPHT ND-O.

Hydrogenation of DNDs is already a well-established process.[44] It was shown that for complete hydrogenation of DNDs in hydrogen gas, a temperature of 600 °C is sufficient.[45–47] However, to fully hydrogenate HPHT NDs, a significantly higher temperature of 750–800 °C is needed as shown recently.[48–50] Thus, to hydrogenate the ND surface DND-ar and HPHT ND-O were annealed in hydrogen gas (flow rate was 5 l min^{-1}) for 6 h at atmospheric pressure at 700 °C for DNDs and 800 °C for HPHT ND.[48] The hydrogenated samples are labelled as DND-H and HPHT ND-H.

2.2 Preparation of ND samples for characterization

Each ND stock colloid was prepared by sonicating 1 mg of a particular ND powder in 1 ml of deionized water in a 2 ml polypropylene test tube using a sonication horn for 1 h at 100 W (Hielscher UP 200s sonicator and S2 titanium sonotrode) in 0.5 s on/off regime. Cooling was ensured by immersing the test tube in a 1 l container filled with cold water. Such prepared colloids were used for DLS measurements and 100 times diluted (to reach 0.01 mg ml^{-1} concentration) for UV-visible spectroscopy measurements. The uniform layers were deposited by spin-coating colloids at 1500 rpm on gold-coated silicon substrates for KP, UPS, and XPS and ITO for ER-EIS measurements. For measurements of work functions of NDs by KP without adsorbates, the samples were annealed in a glove box in a nitrogen atmosphere for 1 h at 250 °C (ref. 14) and then kept in the glove box during all the measurements.

To study the scattering contribution we fractionated the DND-ar stock colloid (Fig. S2†). We extracted a transparent fraction with a DND-ar size range of 10–70 nm by centrifuging (Eppendorf Mini plus) the stock colloid at 14 500 rpm for 1 h, after which 0.8 ml of the supernatant was isolated and characterised by DLS and UV-vis (previously diluted to 0.01 mg ml^{-1}). The fraction with 70–700 nm of DND-ar, which caused turbidity of the DND-ar colloid, was obtained by decanting the stock colloid overnight. Then the supernatant was centrifuged at 14

500 rpm for 3 min. The sediment was isolated and sonicated in 2 ml of water for 10 min using a sonotrode and characterised by DLS and UV-vis (previously diluted to 0.01 mg ml^{-1}).

2.3 Experimental techniques

2.3.1 Fourier transform infrared (FTIR) spectroscopy. Attenuated total reflection-FTIR (ATR-FTIR) analysis was carried out on ND powders using a Nicolet iS50 spectrometer (Thermo Scientific, Nicolet) equipped with a diamond-based ATR accessory. ATR-FTIR spectra for all the samples were recorded at the resolution of 4 cm^{-1} in the range of 400–4000 cm^{-1}. Each spectrum presented here comes as an average of 64 scans. Advanced ATR correction (baseline correction) was performed on all measured spectra using the Omnic software.

2.3.2 Raman spectroscopy. Samples for Raman spectroscopy measurements were prepared by drop casting and drying the ND colloids on Au-coated silicon substrates. By this approach, solid ND deposits were formed and then analysed using a Renishaw InVia system equipped with a 442 nm excitation laser. The laser power did not exceed 1 mW. The acquisition time ranges from 100 to 500 s depending on the signal level. All the spectra were baseline-corrected.

2.3.3 Dynamic light scattering (DLS). DLS measurements of colloidal solutions were performed on a Malvern instrument Zetasizer Nano ZS equipped with a helium–neon laser (633 nm); the scattering angle was 173°. The refractive index of bulk diamond (2.4), and viscosity of pure water (1.0020 mPa s) were used to convert the measured intensity/size distributions to the volume/size distribution. Each sample was analyzed by conducting 6 subsequent runs and a typical DLS curve in between the extremes was chosen as the characteristic one for the particular sample.

2.3.4 UV-vis spectroscopy. Absorbance spectra of the nanodiamond aqueous colloids were measured using a Jasco V 730 spectrometer in the range of 190–800 nm in a quartz cuvette (Hellma 105-10-40) with a 1 cm light path. The accuracy of wavelength measurement of the model is ±0.2 nm (at 656.1 nm). First, ND solutions of concentrations 1, 0.1, 0.01, and 0.001 mg ml^{-1} were characterized resulting in a linear dependence of absorbance on concentration in this range. A concentration of 0.01 mg ml^{-1} was further chosen as the working one since it provided the optimal absorbance value.

The equation $(\alpha h\nu)^2 = A(h\nu - E_g)$, formulated by Tauc[51] and elaborated by Davis and Mott,[52] introduces the coordinates $(\alpha h\nu)^2 - h\nu$ for the determination of the bandgap (E_g) of the amorphous semiconductors (in NDs the crystallinity of the diamond-like core is typically combined with a non-diamond phase which makes the Tauc theory applicable to NDs). The steep linear part of the plot intercepts with the background line of the plot at the point at which (and below) the absorption coefficient is equal to zero, thus, at the value of a bandgap. The uncertainty of bandgap estimation is equal to the sum of uncertainties of the wavelength measurement and linear fit.

Absorption coefficient α is calculated from the Lambert–Beer Law, according to which both absorption and scattering might contribute to the absorbance. The scattering plays a significant role only in DNDs due to the presence of 70–700 nm agglomerate fraction (Fig. S2†) and will be taken into account while determining the E_g of DNDs. Knowing the I_0 and I – the intensities of incoming and outcoming light in the cuvette; d – cuvette side length or the light path length in cm (in our case it was 1 cm); A – absorbance (a.u.),

$$I_0 = e^{-\alpha d} \quad (1)$$

$$\log(I_0) = A \quad (2)$$

By combining eqn (1) and (2) the absorption coefficient can be calculated as follows: $\alpha = 2.303A/d$.

2.3.5 X-ray photoemission spectroscopy (XPS). XPS measurements were conducted in ultra-high vacuum (UHV) at a base pressure in the range of 10^{-10} mbar on films of ND solutions spin-coated on gold substrates and dried at room temperature. We used monochromatized Al Kα excitation (SPECS Focus 500, $E_{excitation} = 1486.71$ eV) for XPS. The photoelectrons were collected in normal emission by a SPECS PHOIBOS 150 hemispherical electron analyzer equipped with a 3D delay line detector (SPECS DLD4040-150).

2.3.6 Ultraviolet photoemission spectroscopy (UPS). The UPS measurements were conducted on drop-cast samples on the gold substrates in UHV at a base pressure in the range of 10^{-10} mbar. P-polarized He Iα excitation (excitation energy 21.22 eV) was used. The photoelectrons were collected using a SPECS PHOIBOS 150 hemispherical electron analyser equipped with a 3D delay line detector (SPECS DLD4040-150).

The work function was determined by (i) fitting a linear function to the slope of the low-energy secondary electron cut-off (SECO) and measuring the intercept with the constant background and (ii) subtracting this cut-off energy from the excitation energy. A bias of ≈ −9 eV was applied to the sample for measuring the SECO and then subtracted from the kinetic energy results. The bias voltage is needed to measure photoelectrons with low kinetic energy since the setup allows the detection of electrons with kinetic energy higher than 5 eV. At very low kinetic energies, the collection and focusing of the photoelectrons on the entrance slit of the hemispherical electron energy analyzer by the electromagnetic lens do not work properly. For a constant electric field to accelerate the photoelectrons and increase their kinetic energy, we need to use a constant voltage source with a bias voltage (the amount of the bias voltage in V corresponds to the change of the kinetic energy in eV). The latter should be high enough to allow measuring samples with a very low work function.

The onset of the valence band was determined by fitting a linear function to the slope of the UPS signal (in the lower energy range of the binding energy coordinates) and measuring the intercept with the constant background. This intercept represents the difference $|E_F - E_V|$. With the known absolute position of the Fermi level (binding energy of 0 eV) and the work function, the position of the valence band relative to the vacuum level was recalculated.[53]

UPS technique is also successfully used to disclose the DOS at the valence band. The disadvantage of the technique in nanodiamond study is the risk of possible surface modification (graphitisation and/or desorption surface functional groups) at UV energies. Therefore, a non-contact and non-spectroscopic method like the Kelvin probe might be advantageous for the work function determination of nanodiamonds.

2.3.7 Kelvin probe (KP). Contact potential difference (CPD) was measured by the Kelvin probe method (KP) (KP Technology 0004) and recalculated to the work function (work function) values using the equation: $WF_{sample} = (CPD_{sample} - CPD_{reference}) \times 10^{-3} + WF_{reference}$

KP measurements were done in a dry nitrogen-filled glove box using a grounded steel probe tip of 2 mm diameter and scanning the sample at 250 points. As the reference, a polished Si sample with thermally evaporated 10 nm of Ti and 150 nm of Au on the top was used.

2.3.8 Energy-resolved electrochemical impedance spectroscopy (ER-EIS). ER-EIS is a novel method of energy level identification and can be considered an alternative to UPS. This method is based on the oxidation–reduction reaction occurring at the interface of an investigated semiconductor film and an electrolyte.[54] The ER-EIS technique was successfully applied to evaluate the electronic structure of nanocrystal thin films as well.[55] ER-EIS measurements were done on nanodiamond films prepared by spin-coating on an ITO substrate using the common three-electrode electrochemical cells (volume of 200 μL). The electrolyte solution consisted of 0.1 M tetrabutylammonium hexafluorophosphate ($TBAPF_6$) in acetonitrile. A potentiostat was used to regulate the potential of the working electrode with respect to the reference Ag/AgCl electrode, and a platinum (Pt) wire served as the counter electrode. Assuming an Ag/AgCl energy *vs.* vacuum value of −4.66 eV, the potential applied with respect to the reference Ag/AgCl electrode can be recalculated to the local vacuum level. The reciprocal value of the real part of the impedance measured at an appropriate frequency provides direct information about the electronic DOS at the energy adjusted by applied voltage. The impedance was measured using a Solartron analytical model 1260 impedance/gain-phase analyzer with a frequency set to 0.5 Hz, and the rms value of the AC voltage of 100 mV. More detailed information on these measurements is provided in the ESI.†

3 Results and discussion

3.1 Surface chemistry and structure of NDs

Before addressing the optoelectronic properties, it is important to highlight structural and chemical differences among the ND samples.

Fig. 1 shows SEM images of HPHT ND-ar (a) and DND-ar (b) which are representative of the HPHT and DND samples, respectively, independent of the surface chemistry. HPHT NDs have a highly irregular shape; still, the distinct faceting of the nanocrystals is noticeable. DNDs' contours are already blurred due to their significantly smaller size. Numerous previous TEM studies showed that the shape of the DND primary particles is roundish with a certain degree of faceting.[56] FTIR and Raman spectroscopies are excellent tools to reveal and describe the important differences in the surface chemistry and structure of the HPHT ND and DND samples. FTIR spectroscopy is a well-established and convenient technique to analyse the ND surface chemistry. Interestingly, recent reports reveal that it can also be applied to investigate electrical conductivity in hydrogenated NDs.[57,58] The FTIR spectra of HPHT ND (Fig. 1c) and DND (Fig. 1d) samples clearly revealed different surface chemistries of the as-received materials, HPHT ND-ar and DND-ar (grey curves), which is obviously due to the different purification treatments performed by the particular manufacturer. HPHT ND-ar sample is characterised by oxygen-rich surface functional groups such as the C=O group (1700–1800 cm^{-1}) and OH groups coming from surface C–OH bonds[59] and/or surface adsorbed water[60] (3000–3700 cm^{-1} OH stretching and ~1630 cm^{-1} OH bending). DND-ar is more polyfunctional, it contains both oxygen-rich moieties and hydrogen-rich moieties. The oxygen-rich moieties involve C=O at 1720 cm^{-1}, complex OH stretching at 3000–3700 cm^{-1} and bending at 1560–1670 cm^{-1}. The sharp peak at 3700 cm^{-1} which also appears in the DND-H spectrum (Fig. 1d, blue) has been associated with the free, non-constrained by hydrogen bonds, OH stretching bonds of the adsorbed water.[14] The hydrogen-rich moieties involve CH_x (2800–3000 cm^{-1}) stretching features. This complex surface chemistry gives this particular DND-ar sample quite specific properties.[31,61] After air oxidation, the surface chemistry of both HPHT ND-O and DND-O became similar and characterised by a strong C=O feature at 1800 cm^{-1} (ref. 62) attributed to carboxylic acid or its anhydride.[63] Due to the negative zeta potential of oxidized NDs (between 30 mV and −40 mV) in deionised water (pH = 5) and the most pronounced FTIR feature at 1800 cm^{-1}, we assume that the carboxylic group is chemically and electronically dominant on the ND-O surfaces.

In contrast, after hydrogenation, the oxygen-rich functional groups are greatly suppressed and the surface chemistry of DND-H and HPHT ND-H is dominated by $-CH_x$ bonds. Note that the greater OH bond contribution in DND-H compared to HPHT ND-H is possibly caused by stronger hydration of DND-H.[48] It has been shown that DND-Hs bind the surface water very tightly even up to 250 °C.[14,61]

Raman spectroscopy further revealed important structural differences between the HPHT ND and DND samples (Fig. 1c and d), namely in the character of the non-diamond phase and the presence of defects in NDs. As highlighted in the recent studies,[64] the DND Raman spectrum is characterised by a broadening and shift of the diamond Raman peak at 1332 cm^{-1} to lower wavenumbers as well as by the appearance of the low-frequency shoulder of the diamond peak due to the highly defective DND structure.[39,40] This includes various point (vacancies, dangling bonds, substitutional nitrogen) and 2D defects (intercrystallite grain boundaries) which (i) decrease the effective coherent scattering domain well below the actual ND size that could be theoretically modelled by phonon confinement models[65] and (ii) may induce heating from the excitation laser due to the increase of optical absorption.[41] In monocrystalline HPHT NDs, no significant shifts of diamond Raman peak have been observed down to 2–3 nm.[6,41]

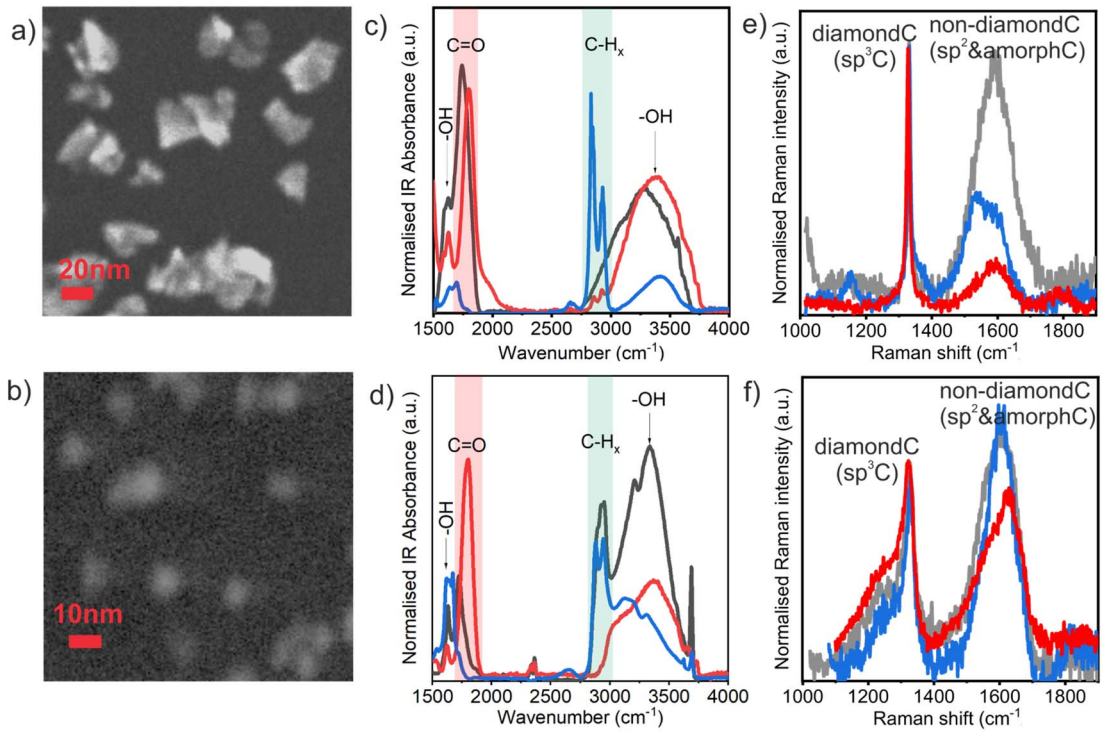

Fig. 1 SEM images of the individual HPHT (a) and DND (b) particles. FTIR spectra of as-received (grey), oxidized (red) and hydrogenated (blue) HPHT (c) and DND (d). Raman spectra of as-received (grey), oxidized (red) and hydrogenated (blue) HPHT (e) and DND (f).

The part of Raman spectra above 1360 cm^{-1} is attributed to the non-diamond carbon and the exact position can be used for distinguishing between different non-diamond carbon forms.[66] HPHT ND-ar has an intense non-diamond C band centred at 1590 cm^{-1} (indicative of graphitic carbon vibrations[66]) that stretches from the amorphous carbon region at ~1520 cm^{-1} (ref. 66) to fragmented sp^2 regions at 1640 cm^{-1}.[66] Such carbon disorder in HPHT ND-ar governs the electronic behaviour of HPHT ND-ar as will be shown further on. The highest graphitic content in HPHT ND-ar clearly correlates with the most intense dark tint of HPHT ND-ar colloidal solution (Fig. S1†). After annealing, the intensity of the non-diamond C band is greatly reduced and only a minor 1590 cm^{-1} component is present in HPHT ND-O (it remains in NDs even down to 5 nm or below) which is attributed to the extended structured sp^2 nanocrystalline graphite-like regions.[66]

After hydrogenation, the peaks of the extended sp^2 phase are present in HPHT ND-H, namely the nanocrystalline graphite peak at 1590 cm^{-1} and 1540 cm^{-1} peak which is assigned to the sp^2 phase in which the bonds between carbon atoms are weakened.[66] Interestingly, the Raman spectrum of the HPHT ND-H contains new features not present in any other NDs. The distinct feature of HPHT ND-H is the presence of *trans*-polyacetylene chains (TPA) which manifest in 1150 and 1450 cm^{-1} (merged in the wide G-band) peaks.[66] The role of TPA in the optoelectronic properties will be discussed further on.

DNDs' non-diamond bands are centred in the ~1600–1630 cm^{-1} range and correspond to fragmented sp^2 regions and isolated sp^2-bonded carbon atoms at the split interstitials.[64] Already purified DNDs are seemingly less sensitive to oxidative thermal treatments compared to HPHT NDs due to the presence of non-diamond C not only on the surface but also in the volume.[56,67] Thus, only a minor surface fraction of it is removed by annealing. Still, in the oxidized DND the sp^2 C is possibly more fragmented (higher wavenumber) than in DND-ar and DND-H which is manifested by the shift of the non-diamond C band from 1600 to 1630 cm^{-1} after DND oxidation in air. The signal at ~1640 cm^{-1} is sometimes attributed to OH vibrations. However, multiple studies showed that the contribution of the surface functional groups in the Raman spectra of DNDs is not significant.[68,69] We also recently showed that the surface chemistry of oxidized DND and HPHT ND in a similar size range (around 5 nm or below) is similar. Yet, their Raman spectra are very different also in the 1620–1640 cm^{-1} spectral range.[41] Thus, we suppose that the 1620–1640 cm^{-1} signal mostly comes from an isolated sp^2-bonded carbon pair defect which occupies the position of one carbon atom in the normal diamond lattice as already suggested by Orwa *et al.*[64]

Thus, despite the similar surface chemistry the NDs of different origins differ in the carbon hybridisation and the nature of the defects which will be reflected in the optoelectronic properties.

3.2 Nanodiamonds' optical bandgaps

Complementary knowledge of ND structure and structural differences is essential for the interpretation of ND absorbance spectra measured by UV-vis spectroscopy. The raw absorption

spectroscopy data are shown in Fig. S3.† For bandgap determination, the absorbance was recalculated to the absorption coefficient and further to the Tauc plots shown in Fig. 2.

The inset image shows the values of the bandgaps of NDs obtained at the point of intercept of the tangent to the Tauc plot and the zero-absorbance line.

Among all the ND samples, HPHT ND-O is characterised by the same optical bandgap value as the bulk diamond electronic bandgap, namely 5.480 ± 0.004 eV.[32] Bandgap values of other HPHT ND samples are lower, namely 5.38 ± 0.01 eV for HPHT ND-ar and 5.21 ± 0.01 eV for HPHT ND-H. The deviation of HPHT ND-ar and HPHT ND-O bandgap value from the bulk diamond bandgap is caused by the non-diamond carbon content that introduces additional energy states into the electronic bandgap as was shown by DFT calculations[20] leading to a decrease in the optical bandgap in NDs depending on the density of these intrabandgap states. Also, Nagata *et al.*[30] observed the decrease of the bandgap in ND-ar using UV-vis spectrometry and explained it with the presence of the $sp^{2+x}C$ phase based on theoretical calculations.[20]

All the DND samples have similar optical bandgap values around ~5.3 eV, independent of the surface chemistry and non-diamond C content, namely 5.30 ± 0.01 eV for DND-H; 5.31 ± 0.01 eV for DND-ar; and 5.31 ± 0.01 eV for DND-O. The formal deviation of DNDs' E_g from bulk diamond E_g is caused by scattering of the 70–700 nm fraction inherently present in DNDs. This fraction causes turbidity of the DND colloids (Fig. S2a†) and increases absorbance (Fig. S2b†) with an apparent bandgap of 5.1 eV (Fig. S2c†).

Since all the dominant size fractions of the used NDs (Fig. S1†) lie above the quantum confinement range which is assumed to appear below 2 nm in NDs,[20] we do not suppose any influence of this effect on the obtained bandgap values.

Thus, for further consideration, we distinguish between the impact of (i) the diamond core sp^3C, and (ii) non-diamond C content on the electronic properties of nanodiamonds. We assign to DNDs and HPHTs under consideration the electronic bandgap of 5.5 eV as if they were pure sp^3C. By doing this we also subtract the effect of scattering on UV-vis measurement in the case of DNDs. The sp^2 and amorphous carbon are taken into account *via* the incorporation of the additional states into the electronic bandgap of NDs as was done in the previous work of Reich.[70]

3.3 Nanodiamonds' valence band maxima (VBM) and the Fermi levels

To construct the NDs' energy diagram, the absolute position of the valence band maxima was determined by UPS (see Fig. 3). UPS spectra in the whole available range of the binding energies (BE) are shown in Fig. 3a. The lower BE energy range of UPS spectra (Fig. 3b) was used to determine the VBM position relative to the Fermi level (E_F). Interestingly, the HPHT ND-H has filled energy states almost to the Fermi level and has the most pronounced photoemission among the other NDs.

The higher BE (*i.e.*, lower kinetic energies) range was used for the determination of the secondary electron cut-off (see Fig. 3c). All ND spectra have a distinct cut-off edge. Then, the Fermi energy level is calculated as E_F (*vs.* vacuum) = $E_{excitation} - E_{cut\text{-}off}$ (Table 1). Clear shifts to higher work function values with surface oxidation happen in both HPHT NDs and DNDs.

Calculated values of the VBM position relative to the vacuum level are presented in Table 1. In general, VBM position highly depends on the ND surface chemistry, namely for the hydrogenated surface it lies in the range −5.0 to −6.3 eV below the vacuum level, while for the oxygenated surfaces, it lies in the range – 7.5–7.8 eV below the vacuum (Table 1).

The trend of the VBM downshift (*vs.* vacuum level) with the introduction of O-containing surface groups follows the trend already reported for carbon materials.[33,71,73] Also, there is a downshift in VBM in HPHT ND-ar (−7.8 ± 0.1 eV) and DND-O (−7.6 ± 0.1 eV) compared to HPHT ND-O (−7.5 ± 0.1 eV). In the former materials, the non-diamond amorphous carbon phase content is higher than in the latter. Thus, the non-diamond amorphous carbon phase causes the downshift of VBM.

Interestingly, the HPHT ND-H valence band maximum is upshifted to −5.0 eV relative to the vacuum level. It lies in the range of VBMs of materials suitable for hole extraction at the heterojunction. This makes HPHT ND-H a prospective charge-transfer material in photovoltaics. Moreover, the ambient adsorbate O_2/H_2O with electrochemical level −5.3 eV (at ambient pH 6) *vs.* vacuum can p-dope the surface of HPHT ND-H with VBM at −5.0 eV, making the nanoparticle positively charged and possibly conductive as it was observed for hydrogenated microcrystalline diamond[74] and bulk diamond.[75] In general, any adsorbate with an electrochemical level below −5.0 eV supposedly p-dopes HPHT ND-H. The phenomenon of surface conductivity due to reversible electrochemical

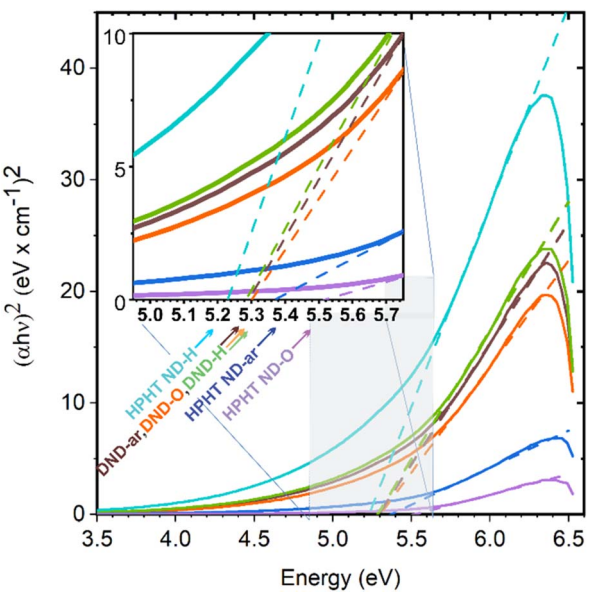

Fig. 2 Tauc plots of the investigated ND samples. Absorption coefficient α was determined from UV-vis absorbance spectra. The inset's pointed values are NDs' bandgaps estimated from the intersections of the tangent to the Tauc plot and zero absorption coefficient line.

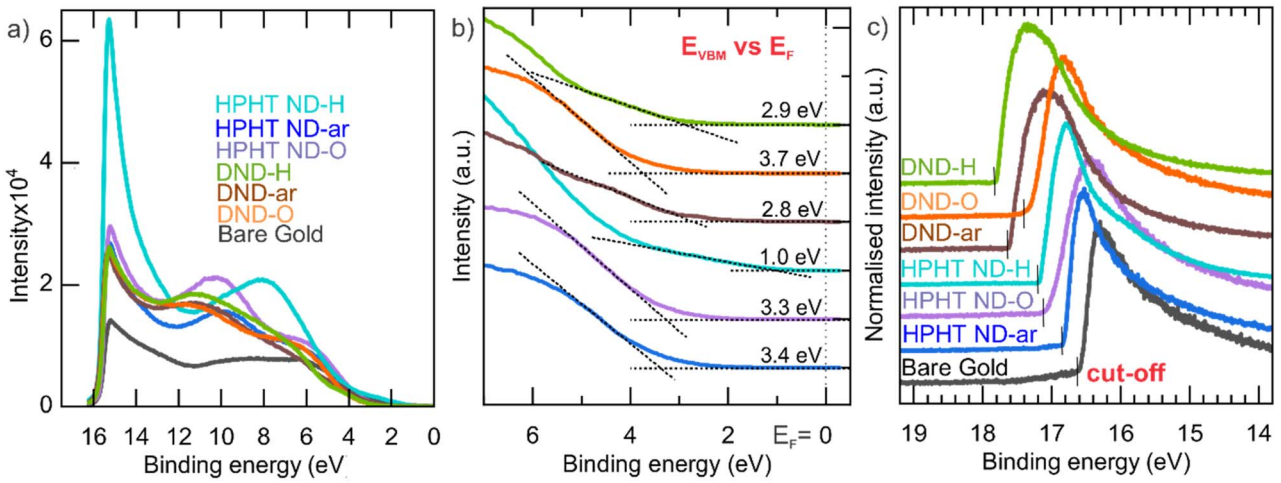

Fig. 3 (a) UPS spectra in the whole energy range; (b) zoomed-in valence band onset region of UPS spectra relative to the E_F; (c) zoomed-in cut-off energy region for determination of E_F *vs.* vacuum.

Table 1 Calculated E_F and E_V from the UPS spectra relative to the vacuum level

Material	E_F *vs.* vacuum, eV	$\lvert E_F - E_{VBM}\rvert$, eV	E_{VBM} *vs.* vacuum, eV
HPHT ND-H	-4.0 ± 0.1	1.0 ± 0.1	-5.0 ± 0.1
HPHT ND-ar	-4.4 ± 0.1	3.4 ± 0.1	-7.8 ± 0.1
HPHT ND-O	-4.2 ± 0.1	3.3 ± 0.1	-7.5 ± 0.1
DND-H	-3.4 ± 0.1	2.9 ± 0.1	-6.3 ± 0.1
DND-ar	-3.4 ± 0.1	2.8 ± 0.1	-6.2 ± 0.1
DND-O	-3.9 ± 0.1	3.7 ± 0.1	-7.6 ± 0.1

interaction between the semiconductor surface and its adsorbate which is enabled by the higher position of the valence band maximum of the semiconductor relative to the electrochemical level of the adsorbate is known as the surface transfer doping[76,77] and was described first by Maier.[78] P-doping due to high VBM can significantly contribute to the positive zeta potential of ND-H.[22]

After compiling the results of UV-vis and UPS measurements, we constructed the energy level diagrams of HPHT ND and DND of as-received, hydrogenated, and oxidized surfaces (Scheme 1). On the vertical energy scale VBM, CBM (calculated as VBM + bandgap), and Fermi level are presented. The diagram clearly shows the downshift of VBM and Fermi level (*vs.* vacuum level) independently after oxidation and the presence of sp^2 and amorphous carbon phases.

The diagram presents a striking difference in HPHT ND-H compared to other NDs, namely the high VBM of HPHT ND-H, which, combined with the bandgap value, locates the conduction band minimum (CBM) to +0.5 eV above vacuum. This results in the negative electron affinity (or NEA) of HPHT ND-H with important electrochemical consequences, such as the possibility of electron ejection into molecules such as water (CBM of water at ~ -0.8 eV below the vacuum level) and nitrogen (CBM at -0.2 eV below the vacuum level).[79] The facilitation of electron ejection by HPHT ND-H compared to other NDs is also supported by XPS measurements (Fig. S4†). Interestingly, DND-Hs with the same surface chemistry as HPHT ND-H do not have the NEA most probably due to different non-diamond carbon forms in these materials that lead to different electronic properties. Other parameters such as size or shape do not significantly affect the presence or absence of NEA in this case. The specific crystallographic orientation of the hydrogenated diamond surface does influence the actual NEA value, but not its presence.[80,81] Hydrogenated nanocrystalline diamond thin films with multifaceted and variously shaped nanoscale grains of different mean sizes, 80 and 250 nm, can be a good illustration for this since the NEA was present in all these films and allowed the operation of field-effect transistors.[82] Effects such as a more defective structure and 2 at% of embedded N in DND-H may influence its conductivity and other electronic properties, but NEA is solely a property due to C–H bonds on the diamond surface.[80,81] Therefore, we believe that the missing NEA on DND-H must be related to the non-diamond (namely, amorphous carbon) character of its surface despite the C–H bond termination of DND-H.

It should be notified that depending on the characterisation method and the presence of airborne adsorbates on the ND surfaces, work function values of the same ND sample might vary. Fig. 4a compares the work function obtained by the Kelvin probe (KP) and UPS. For HPHT NDs the work function values estimated by both techniques are similar. For DNDs, the work function by UPS appears to be systematically 0.7–0.9 eV lower compared to the work function obtained by KP. It could be due to the different responsiveness of DNDs to UV light compared to HPHTs. Also, the more pronounced curvature of DNDs compared to HPHT NDs could weaken the binding of π-electrons to the material leading to a decrease in the work function in UPS.[73]

The trend of an increasing work function with increasing O content on the ND surface revealed by KP is consistent with the studies of the oxygenation impact on the work function in different materials[72] and can be explained by the formation of

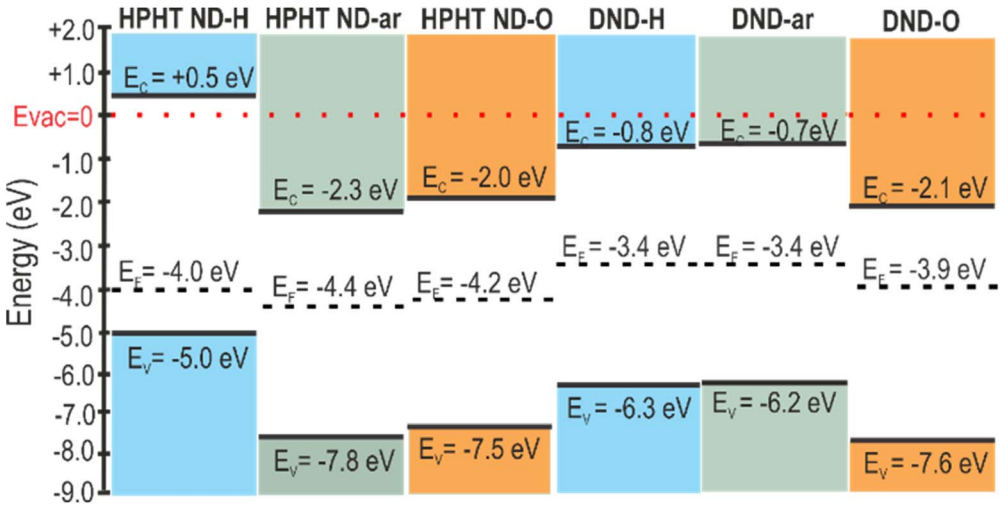

Scheme 1 Band diagrams of HPHT and DND nanodiamonds of as-received, hydrogenated, and oxidized surfaces.

CO dipoles which form the additional barrier for the electrons and thereby increasing the work function. The impact of the ambient adsorbates on NDs' work function Fig. 4b, namely O_2/H_2O, is very pronounced for HPHT ND-H. It confirms the electrochemical reaction between the high VBM of HPHT ND-H and the electrochemical level of the adsorbate species mentioned earlier. Such interactions can lead to an electron transfer from HPHT ND-H to O_2/H_2O, p-doping of ND and a subsequent downshift of the Fermi level with respect to the vacuum level equal to an increase of the work function that is clearly seen in Fig. 4b. The VBM position downshift relative to the Fermi level after heating was only about 0.3 eV compared to the VBM of the HPHT ND-H sample saturated with the ambient adsorbates (see Fig. S5†). The minor change of VBM in different environments could be explained by band bending due to the interaction of the HPHT ND-H surface with the adsorbates in the ambient.

3.4 The density of states (DOS) in nanodiamonds

The mapping of electronic states was performed with the ER-EIS technique, in which ER-EIS spectra directly reflect the DOS of ND layers. Fig. 5 shows the DOS spectra of the as-received, fully hydrogenated (reduced), and fully oxidized ND layers along with the reference spectra of the bare ITO substrate.

The reference spectra are needed to distinguish the contribution of the investigated material itself and the substrate into DOS. In HPHT ND-H there is a pronounced DOS increase from −5.0 eV and below, indicating the VBM at −5.0 eV (Fig. 5a). This is in excellent agreement with the UPS results of the VBM value (−5.0 eV). Besides, there are additional electronic states in the bandgap of HPHT ND-H that are delocalised up to ∼−3 eV. From −3.0 eV to −2.6 eV there is a gap and above it, there is a method limitation. DFT calculations show that the sp^2 phase on the ND surface introduces electronic states into the bandgap leading to the narrowing of the bandgap.[83] Also, this ER-EIS result is in good agreement with UPS non-zero photoemission in the range between the Fermi level and VBM found in HPHT ND-H. Furthermore, the delocalisation of electronic states in HPHT ND-H can explain the conductivity of HPHT ND-H that distinguishes it from the other NDs.[15]

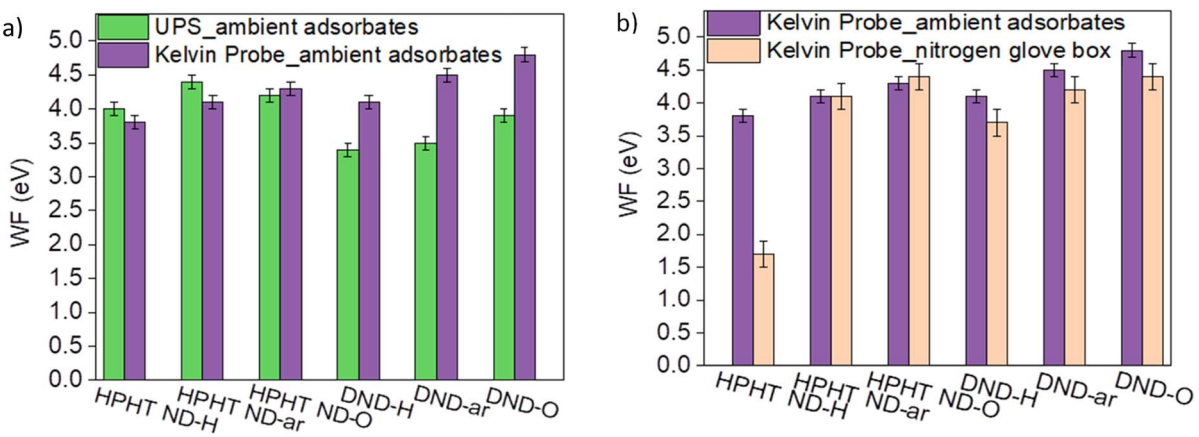

Fig. 4 Comparison of WF work functions determined by (a) KP and UPS; (b) KP with and without ambient adsorbates.

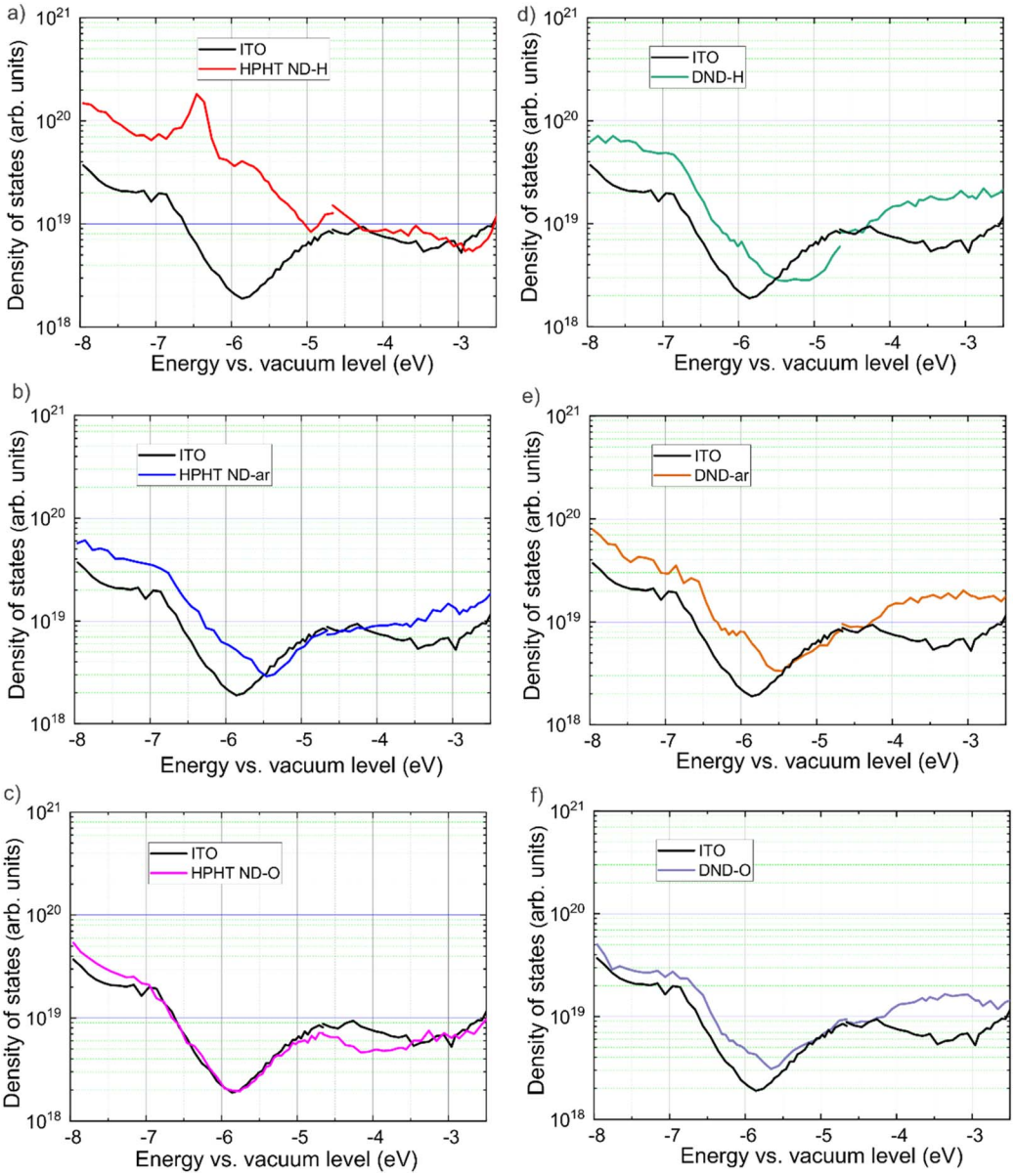

Fig. 5 Band diagrams of HPHT and DND layers of NDs with as-received, hydrogenated, and oxidized surfaces obtained with the ER-EIS. DOS profiles are measured in the energy range from −8.0 to −2.5 eV (this is the limitation of the ER-EIS technique). The DOS of the ITO substrate is a black curve.

In HPHT ND-ar a steep exponential increase of the density of states in HPHT ND-ar compared to the substrate is observed between −5.5 eV and −6.8 eV. The exponential increase continues from −6.8 to −8.0 eV, however, it takes a less steep slope (Fig. 5b). Based on ER-EIS we can assign VBM either to −5.5 eV or −6.8 eV. Both values are higher than UPS VBM for HPHT ND-ar (−7.8 eV). In this regard, they also might originate from the intrabandgap electronic states caused by non-diamond C while the UPS VBM of HPHT ND-ar lies out of the energy range of the ER-EIS method.

In the spectrum of HPHT ND-O (Fig. 5c) no additional electronic states in the bandgap are present (at least until the measurement technique limit) which is obviously due to the low non-diamond content compared to HPHT ND-ar (in agreement with Raman spectra in Fig. 1). Moreover, HPHT ND-O even passivates the electronic states in the substrate (the DOS of HPHT ND-O on ITO goes below the DOS of bare ITO). The absence of the delocalised states in HPHT ND-O can explain the insulating properties of this material.[15] The exponential increase of DOS at −7.0 eV of HPHT ND-O indicates the VBM position which reasonably agrees with the VBM determined *via* UPS (−7.5 eV).

Interestingly, ER-EIS spectra in the intrabandgap region of all the DNDs (Fig. 5d–f) look similar to each other and HPHT ND-ar. Raman spectra showed that the amorphous and isolated sp^2 carbon fragments are a common structural feature in these

samples. Most probably intrabandgap DOS in DNDs and HPHT ND-ar is dominated by amorphous carbon contribution while surface chemistry seems to have only a minor impact on these electronic states of DNDs in the ER-EIS measurements. As part of our future work, we are corroborating data differently by preparing a publication focusing solely on ER-EIS DOS data and calculated *via* density functional theory DOS of the ND models with the predefined surface groups to elucidate more strictly the effect of surface structure on the DOS of NDs.

3.5 Structure–electronic property relationships in nanodiamonds

After projecting the surface chemistry and carbon hybridisation states on the band diagram of the NDs, the regularities in electronic level shifts for NDs of different origins and surfaces are revealed (see Scheme 2). In Scheme 2 the following simplified classification is adopted, namely, sp^3-Cbulk-H/-O refer to the bulk diamond in which C is solely sp^3 hybridised and surface dangling bonds are saturated by H or O atoms. The values of the energy levels for the bulk diamond are taken from the literature.[81,84] In the studied NDs there is always some fraction of non-diamond C due to fabrication (DND) and processing (DND and HPHT ND). In HPHT ND-H the non-diamond C is represented by an ordered sp^2 C (see Fig. 1e and discussion), with the significant contribution of *trans*-polyacetylene chains; thus, {sp^3ND + sp^2C}-H depicts the structure and surface chemistry of HPHT ND-H (brackets in the label denote the hydrogenation/oxidation of both sp^3ND and sp^2C regions). DND-H contains a large amount of amorphous carbon (aC) in its structure whose impact on the optoelectronic properties of DND-H is significant according to ER-EIS. Thus, {sp^3ND + aC}-H describes the structure and surface chemistry of DND-H. In oxidized species, the surface of HPHT ND-O differs from oxidized bulk diamond surface by the presence of the ordered sp^2 phase. Thus, {sp^3ND + sp^2C}-O depicts the structure and surface chemistry of HPHT ND-O. The more defective nature of DND-O and HPHT ND-ar with pronounced amorphous C content is denoted as {sp^3ND + aC}-O. DND-ar with the mixture of oxygen and hydrogen groups, and surface and volume defects are taken out of this classification so as not to complicate the picture.

One of the trends in the energy levels' positions (VBM, CBM, E_F) observed is several-eV (1.3–2.5 eV depending on the origin of the nanodiamonds) VBM downshift relative to the vacuum level after conversion from the fully hydrogenated to the fully oxidized surface (VBM downshifts in pairs HPHT ND-H and HPHT ND-O; DND-H and DND-O). Moreover, a clear effect of the carbon hybridization (ND structure) is observed. For the defined surface chemistry (H/O), the presence of non-diamond carbon downshifts the band edges compared to purely sp^3 carbon hybridization in diamonds (compare energy levels of the bulk diamond with the ones of the materials with non-diamond C in Scheme 2). Notably, amorphous non-diamond C compared to the ordered sp^2 C downshifts the ND band edges relative to the vacuum level by 0.1–1.3 eV depending on ND origin and surface chemistry (compare the VBM of both oxidized HPHT ND-O with structured sp^2 and HPHT ND-ar with amorphous non-diamond C; hydrogenated HPHT ND-H with *trans*-polyacetylene chains and DND-H with amorphous non-diamond C).

Thus, the described edge energy level position with the knowledge of work function variation and DOS can facilitate the selection of suitable materials for such applications as photovoltaics and catalysis. Moreover, our experimental results provide evidence for the recent theoretical results on structured sp^2 origin of continuous intrabandgap states[83] and quantitative backup for the experimental studies on charge transfer in nanodiamond composites[23,31] and resolve the discrepancies between the published results on ND optoelectronic properties (*e.g.* ND apparent bandgap differences[30,85]).

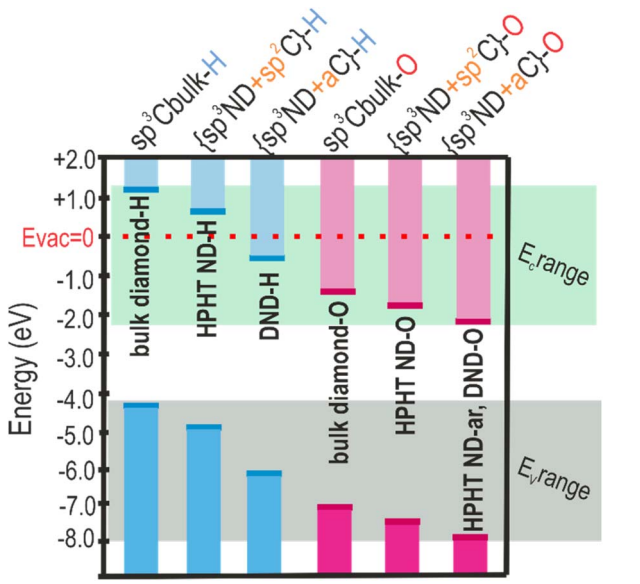

Scheme 2 Simplified band energy position dependence on surface chemistry and C-hybridization of NDs.

4 Conclusions

This work brings a comprehensive and quantitative approach to the understanding of the electronic properties of HPHT and detonation nanodiamonds with hydrogenated and oxidized surfaces. Band edges, the density of states, and work functions are determined purely experimentally by combining various spectroscopic methods, Kelvin probe and electrochemical impedance spectroscopy. The obtained data show that the positioning of the VBM of HPHT ND-H is high enough (−5.0 eV relative to the vacuum level), which together with the wide bandgap of NDs, assures that the CBM is positioned above the vacuum level (+0.5 eV). This way the NEA of HPHT ND-H is justified. Interestingly, HPHT ND-H contains the continuum of the electronic states inside the bandgap that, in addition to transfer doping, can contribute to electrical conductivity. We propose that a conjugated sp^2 phase such as the *trans*-polyacetylene indicated by Raman spectroscopy introduces the intrabandgap states. DND-H does not possess NEA. We explain such a difference by the presence of amorphous carbon in DND-H that downshifts the VBM in DND-H compared to HPHT ND-H

introducing positive electron affinity. The downshift of VBM relative to the vacuum level after amorphisation of the ND surface is in the 0.1–1.3 eV range (depending on the ND origin and surface chemistry) and after the fully hydrogenated surface oxidation it is in the 1.3–2.5 eV range (depending on the ND origin). The results can serve as a guide for selecting the suitable ND material for a particular application among the variety of NDs that differ in origin, surface chemistry and non-diamond carbon quality and content. For example, our work suggests that HPHT ND-H can be used for the photoreduction of N_2 to ammonia and the production of solvated electrons in aqueous solutions. Also, this material combining high VBM with consequent high CBM *vs.* vacuum and electrical conductivity could find its application as a charge transport material in photovoltaics.

Author contributions

DM conceptualisation, methodology, investigation, data & model visualisation, writing original draft; ASD – research discussion, manuscript review; JC – funding acquisition, manuscript review & editing; MS, FO and OR – UPS and XPS analysis, formal analysis and data visualisation review & editing; ES – FTIR; JP – hydrogenation of NDs; JK – Kelvin probe; VN – ER-EIS, formal analysis and data visualisation; SS – resources, research discussion, manuscript review & editing, funding acquisition; AK – resources, funding acquisition, manuscript review; HH – resources, research discussion, manuscript review & editing; BR – resources, research discussion, data processing and visualization, manuscript review & editing.

Conflicts of interest

There are no conflicts of interest to declare.

Acknowledgements

This work has been financially supported by the Czech Science Foundation project 20-20991J (GACR), the European Regional Development Fund project CZ.02.1.01/0.0/0.0/15 003/0000464 (CAP), and the Deutsche Forschungsgemeinschaft (DFG) *via* the DFG project number 431903417. We also acknowledge the use of the CzechNanoLab research infrastructure supported by the MEYS (LM2023051).

References

1 A. Krueger and D. Lang, *Adv. Funct. Mater.*, 2012, **22**, 890–906.
2 V. N. Mochalin, O. Shenderova, D. Ho and Y. Gogotsi, *Nat. Nanotechnol.*, 2012, **7**, 11–23.
3 N. Nunn, M. Torelli, G. McGuire and O. Shenderova, *Curr. Opin. Solid State Mater. Sci.*, 2017, **21**, 1–9.
4 L. Schmidlin, V. Pichot, M. Comet, S. Josset, P. Rabu and D. Spitzer, *Diamond Relat. Mater.*, 2012, **22**, 113–117.
5 W. S. Yeap, S. Chen and K. P. Loh, *Langmuir*, 2009, **25**, 185–191.
6 A. Vlk, M. Ledinsky, A. Shiryaev, E. Ekimov and S. Stehlik, *J. Phys. Chem. C*, 2022, **126**, 6318–6324.
7 J.-P. Boudou, J. Tisler, R. Reuter, A. Thorel, P. A. Curmi, F. Jelezko and J. Wrachtrup, *Diamond Relat. Mater.*, 2013, **37**, 80–86.
8 S. V. Bolshedvorskii, A. I. Zeleneev, V. V. Vorobyov, V. V. Soshenko, O. R. Rubinas, L. A. Zhulikov, P. A. Pivovarov, V. N. Sorokin, A. N. Smolyaninov, L. F. Kulikova, A. S. Garanina, S. G. Lyapin, V. N. Agafonov, R. E. Uzbekov, V. A. Davydov and A. V. Akimov, *ACS Appl. Nano Mater.*, 2019, **2**, 4765–4772.
9 V. A. Shershulin, V. S. Sedov, A. Ermakova, U. Jantzen, L. Rogers, A. A. Huhlina, E. G. Teverovskaya, V. G. Ralchenko, F. Jelezko and I. I. Vlasov, *Phys. Status Solidi A*, 2015, **212**, 2600–2605.
10 N. Gibson, O. Shenderova, T. J. M. Luo, S. Moseenkov, V. Bondar, A. Puzyr, K. Purtov, Z. Fitzgerald and D. W. Brenner, *Diamond Relat. Mater.*, 2009, **18**, 620–626.
11 H. Huang, E. Pierstorff, E. Osawa and D. Ho, *Nano Lett.*, 2007, **7**, 3305–3314.
12 R. A. Shimkunas, E. Robinson, R. Lam, S. Lu, X. Xu, X.-Q. Zhang, H. Huang, E. Osawa and D. Ho, *Biomaterials*, 2009, **30**, 5720–5728.
13 B. S. Miller, L. Bezinge, H. D. Gliddon, D. Huang, G. Dold, E. R. Gray, J. Heaney, P. J. Dobson, E. Nastouli, J. J. L. Morton and R. A. McKendry, *Nature*, 2020, **587**, 588–593.
14 S. Stehlik, T. Glatzel, V. Pichot, R. Pawlak, E. Meyer, D. Spitzer and B. Rezek, *Diamond Relat. Mater.*, 2016, **63**, 97–102.
15 J. Čermák, H. Kozak, Š. Stehlík, V. Švrček, V. Pichot, D. Spitzer, A. Kromka and B. Rezek, *MRS Adv.*, 2016, **1**, 1105–1111.
16 J. B. Cui, J. Ristein and L. Ley, *Phys. Rev. Lett.*, 1998, **81**, 429–432.
17 F. Maier, J. Ristein and L. Ley, *Phys. Rev. B: Condens. Matter Mater. Phys.*, 2001, **64**, 165411.
18 J. Ristein, *Surf. Sci.*, 2006, **600**, 3677–3689.
19 C. A. Feigl, B. Motevalli, A. J. Parker, B. Sun and A. S. Barnard, *Nanoscale Horiz.*, 2019, **4**, 983–990.
20 F. Buchner, T. Kirschbaum, A. Venerosy, H. Girard, J.-C. Arnault, B. Kiendl, A. Krueger, K. Larsson, A. Bande, T. Petit and C. Merschjann, *Nanoscale*, 2022, **14**, 17188–17195.
21 X. Duan, W. Tian, H. Zhang, H. Sun, Z. Ao, Z. Shao and S. Wang, *ACS Catal.*, 2019, **9**, 7494–7519.
22 L. Ginés, S. Mandal, A.-I.-A. Ashek-I-Ahmed, C.-L. Cheng, M. Sow and O. A. Williams, *Nanoscale*, 2017, **9**, 12549–12555.
23 J. Henych, Š. Stehlík, K. Mazanec, J. Tolasz, J. Čermák, B. Rezek, A. Mattsson and L. Österlund, *Appl. Catal., B*, 2019, **259**, 118097.
24 D. M. Jang, Y. Myung, H. S. Im, Y. S. Seo, Y. J. Cho, C. W. Lee, J. Park, A.-Y. Jee and M. Lee, *Chem. Commun.*, 2012, **48**, 696–698.
25 H. Wang, Y.-K. Tzeng, Y. Ji, Y. Li, J. Li, X. Zheng, A. Yang, Y. Liu, Y. Gong, L. Cai, Y. Li, X. Zhang, W. Chen, B. Liu,

H. Lu, N. A. Melosh, Z.-X. Shen, K. Chan, T. Tan, S. Chu and Y. Cui, *Nat. Nanotechnol.*, 2020, **15**, 131–137.
26 S. Yu, N. Yang, H. Zhuang, J. Meyer, S. Mandal, O. A. Williams, I. Lilge, H. Schönherr and X. Jiang, *J. Phys. Chem. C*, 2015, **119**, 18918–18926.
27 Y. Liu, Y.-K. Tzeng, D. Lin, A. Pei, H. Lu, N. A. Melosh, Z.-X. Shen, S. Chu and Y. Cui, *Joule*, 2018, **2**, 1595–1609.
28 K. Jothiramalingam Sankaran, S. Kunuku, B. Sundaravel, P.-Y. Hsieh, H.-C. Chen, K.-C. Leou, N.-H. Tai and I.-N. Lin, *Nanoscale*, 2015, **7**, 4377–4385.
29 Y. L. Zhong, A. Midya, Z. Ng, Z.-K. Chen, M. Daenen, M. Nesladek and K. P. Loh, *J. Am. Chem. Soc.*, 2008, **130**, 17218–17219.
30 A. Nagata, O. K. U. Takeo, K. Kikuchi, A. Suzuki, Y. Yamasaki and E. Osawa, *Prog. Nat. Sci.*, 2010, **20**, 38–43.
31 D. Miliaieva, P. Matunova, J. Cermak, S. Stehlik, A. Cernescu, Z. Remes, P. Stenclova, M. Muller and B. Rezek, *Sci. Rep.*, 2021, **11**, 590.
32 L. Cheng, S. Zhu, X. Ouyang and W. Zheng, *Diamond Relat. Mater.*, 2023, **132**, 109638.
33 T. Kondo, I. Neitzel, V. N. Mochalin, J. Urai, M. Yuasa and Y. Gogotsi, *J. Appl. Phys.*, 2013, **113**, 214307.
34 K.-Y. Niu, H.-M. Zheng, Z.-Q. Li, J. Yang, J. Sun and X.-W. Du, *Angew. Chem.*, 2011, **123**, 4185–4188.
35 P. Matunová, V. Jirásek and B. Rezek, *Phys. Status Solidi B*, 2019, 1900176.
36 A. A. Fokin and P. R. Schreiner, *Mol. Phys.*, 2009, **107**, 823–830.
37 S. Osswald, G. Yushin, V. Mochalin, S. O. Kucheyev and Y. Gogotsi, *J. Am. Chem. Soc.*, 2006, **128**, 11635–11642.
38 V. I. Korepanov, H. Hamaguchi, E. Osawa, V. Ermolenkov, I. K. Lednev, B. J. M. Etzold, O. Levinson, B. Zousman, C. P. Epperla and H.-C. Chang, *Carbon*, 2017, **121**, 322–329.
39 S. Osswald, M. Havel, V. Mochalin, G. Yushin and Y. Gogotsi, *Diamond Relat. Mater.*, 2008, **17**, 1122–1126.
40 S. Stehlik, M. Varga, M. Ledinsky, D. Miliaieva, H. Kozak, V. Skakalova, C. Mangler, T. J. Pennycook, J. C. Meyer, A. Kromka and B. Rezek, *Sci. Rep.*, 2016, **6**, 38419.
41 S. Stehlik, M. Mermoux, B. Schummer, O. Vanek, K. Kolarova, P. Stenclova, A. Vlk, M. Ledinsky, R. Pfeifer, O. Romanyuk, I. Gordeev, F. Roussel-Dherbey, Z. Nemeckova, J. Henych, P. Bezdicka, A. Kromka and B. Rezek, *J. Phys. Chem. C*, 2021, **125**, 5647–5669.
42 V. I. Korepanov, H. Hamaguchi, E. Osawa, V. Ermolenkov, I. K. Lednev, B. J. M. Etzold, O. Levinson, B. Zousman, C. P. Epperla and H.-C. Chang, *Carbon*, 2017, **121**, 322–329.
43 K. Turcheniuk and V. N. Mochalin, *Nanotechnology*, 2017, **28**, 252001.
44 O. A. Williams, J. Hees, C. Dieker, W. Jäger, L. Kirste and C. E. Nebel, *ACS Nano*, 2010, **4**, 4824–4830.
45 T. Kondo, I. Neitzel, V. N. Mochalin, J. Urai, M. Yuasa and Y. Gogotsi, *J. Appl. Phys.*, 2013, **113**, 214307.
46 A.-I. Ahmed, S. Mandal, L. Gines, O. A. Williams and C.-L. Cheng, *Carbon*, 2016, **110**, 438–442.
47 S. Stehlik, M. Varga, P. Stenclova, L. Ondic, M. Ledinsky, J. Pangrac, O. Vanek, J. Lipov, A. Kromka and B. Rezek, *ACS Appl. Mater. Interfaces*, 2017, **9**, 38842–38853.
48 J. Mikesova, D. Miliaieva, P. Stenclova, M. Kindermann, T. Vuckova, M. Madlikova, M. Fabry, V. Veverka, J. Schimer, P. Krejci, S. Stehlik and P. Cigler, *Carbon*, 2022, **195**, 372–386.
49 L. Saoudi, H. A. Girard, E. Larquet, M. Mermoux, J. Leroy and J.-C. Arnault, *Carbon*, 2023, **202**, 438–449.
50 K. Kolarova, I. Bydzovska, O. Romanyuk, E. Shagieva, E. Ukraintsev, A. Kromka, B. Rezek and S. Stehlik, *Diamond Relat. Mater.*, 2023, 109754.
51 J. Tauc, R. Grigorovici and A. Vancu, *Phys. Status Solidi B*, 1966, **15**, 627–637.
52 E. A. Davis and N. F. Mott, *Philos. Mag.*, 1970, **22**, 0903–0922.
53 A. M. Shing, Y. Tolstova, N. S. Lewis and H. A. Atwater, *Appl. Phys. A*, 2017, **123**, 735.
54 V. Nádaždy, F. Schauer and K. Gmucová, *Appl. Phys. Lett.*, 2014, **105**, 142109.
55 S. Volk, N. Yazdani, E. Sanusoglu, O. Yarema, M. Yarema and V. Wood, *J. Phys. Chem. Lett.*, 2018, **9**, 1384–1392.
56 S. Turner, O. Shenderova, F. D. Pieve, Y. Lu, E. Yücelen, J. Verbeeck, D. Lamoen and G. V. Tendeloo, *Phys. Status Solidi A*, 2013, **210**, 1976–1984.
57 O. S. Kudryavtsev, R. H. Bagramov, A. M. Satanin, A. A. Shiryaev, O. I. Lebedev, A. M. Romshin, D. G. Pasternak, A. V. Nikolaev, V. P. Filonenko and I. I. Vlasov, *Nano Lett.*, 2022, **22**, 2589–2594.
58 E. Ekimov, A. A. Shiryaev, Y. Grigoriev, A. Averin, E. Shagieva, S. Stehlik and M. Kondrin, *Nanomaterials*, 2022, **12**, 351.
59 A. Wolcott, T. Schiros, M. E. Trusheim, E. H. Chen, D. Nordlund, R. E. Diaz, O. Gaathon, D. Englund and J. S. Owen, *J. Phys. Chem. C*, 2014, **118**, 26695–26702.
60 S. Ji, T. Jiang, K. Xu and S. Li, *Appl. Surf. Sci.*, 1998, **133**, 231–238.
61 T. Petit, L. Puskar, T. Dolenko, S. Choudhury, E. Ritter, S. Burikov, K. Laptinskiy, Q. Brzustowski, U. Schade, H. Yuzawa, M. Nagasaka, N. Kosugi, M. Kurzyp, A. Venerosy, H. Girard, J.-C. Arnault, E. Osawa, N. Nunn, O. Shenderova and E. F. Aziz, *J. Phys. Chem. C*, 2017, **121**, 5185–5194.
62 S. Stehlik, M. Varga, M. Ledinsky, V. Jirasek, A. Artemenko, H. Kozak, L. Ondic, V. Skakalova, G. Argentero, T. Pennycook, J. C. Meyer, A. Fejfar, A. Kromka and B. Rezek, *J. Phys. Chem. C*, 2015, **119**, 27708–27720.
63 A. P. Koshcheev, *Russ. J. Gen. Chem.*, 2009, **79**, 2033–2044.
64 J. O. Orwa, K. W. Nugent, D. N. Jamieson and S. Prawer, *Phys. Rev. B: Condens. Matter Mater. Phys.*, 2000, **62**, 5461–5472.
65 S. Osswald, V. N. Mochalin, M. Havel, G. Yushin and Y. Gogotsi, *Phys. Rev. B: Condens. Matter Mater. Phys.*, 2009, **80**, 075419.
66 A. C. Ferrari and J. Robertson, *Philos. Trans. R. Soc., A*, 2004, **362**, 2477–2512.
67 S. Turner, O. I. Lebedev, O. Shenderova, I. I. Vlasov, J. Verbeeck and G. Van Tendeloo, *Adv. Funct. Mater.*, 2009, **19**, 2116–2124.
68 M. Mermoux, A. Crisci, T. Petit, H. A. Girard and J.-C. Arnault, *J. Phys. Chem. C*, 2014, **118**, 23415–23425.
69 M. Mermoux, S. Chang, H. A. Girard and J.-C. Arnault, *Diamond Relat. Mater.*, 2018, **87**, 248–260.

70 K. V. Reich, *JETP Lett.*, 2011, **94**, 22.
71 H. K. Jeong, C. Yang, B. S. Kim and K. Kim, *Europhys. Lett.*, 2010, **92**, 37005.
72 J. C. Zuaznabar-Gardona and A. Fragoso, *Synth. Met.*, 2020, **266**, 116434.
73 H. Ago, T. Kugler, F. Cacialli, W. R. Salaneck, M. S. P. Shaffer, A. H. Windle and R. H. Friend, *J. Phys. Chem. B*, 1999, **103**, 8116–8121.
74 V. Chakrapani, J. C. Angus, A. B. Anderson, S. D. Wolter, B. R. Stoner and G. U. Sumanasekera, *Science*, 2007, **318**, 1424–1430.
75 C. E. Nebel, *Science*, 2007, **318**, 1391–1392.
76 W. Chen, D. Qi, X. Gao and A. T. S. Wee, *Prog. Surf. Sci.*, 2009, **84**, 279–321.
77 K. G. Crawford, I. Maini, D. A. Macdonald and D. A. J. Moran, *Prog. Surf. Sci.*, 2021, **96**, 100613.
78 F. Maier, M. Riedel, B. Mantel, J. Ristein and L. Ley, *Phys. Rev. Lett.*, 2000, **85**, 3472–3475.
79 N. Bauer, *J. Phys. Chem.*, 1960, **64**, 833–837.
80 J. B. Cui, J. Ristein and L. Ley, *Phys. Rev. Lett.*, 1998, **81**, 429–432.
81 F. Maier, J. Ristein and L. Ley, *Phys. Rev. B: Condens. Matter Mater. Phys.*, 2001, **64**, 165411.
82 M. Krátká, A. Kromka, E. Ukraintsev, M. Ledinský, A. Brož, M. Kalbacova and B. Rezek, *Sens. Actuators, B*, 2012, **166–167**, 239–245.
83 F. Buchner, T. Kirschbaum, A. Venerosy, H. Girard, J.-C. Arnault, B. Kiendl, A. Krueger, K. Larsson, A. Bande, T. Petit and C. Merschjann, *Nanoscale*, 2022, **14**, 17188–17195.
84 C. E. Nebel, B. Rezek, D. Shin and H. Watanabe, *Phys. Status Solidi A*, 2006, **203**, 3273–3298.
85 N. Giambrone, M. McCrory, A. Kumar and M. K. Ram, *Thin Solid Films*, 2016, **615**, 226–232.